

# Catalogue of topological electronic materials

Tiantian Zhang<sup>1,2,9</sup>, Yi Jiang<sup>1,2,9</sup>, Zhida Song<sup>1,2,9</sup>, He Huang<sup>3</sup>, Yuqing He<sup>2,3</sup>, Zhong Fang<sup>1,4</sup>, Hongming Weng<sup>1,5,6,7,8\*</sup> & Chen Fang<sup>1,4,6,7,8\*</sup>

**Topological electronic materials such as bismuth selenide, tantalum arsenide and sodium bismuthide show unconventional linear response in the bulk, as well as anomalous gapless states at their boundaries. They are of both fundamental and applied interest, with the potential for use in high-performance electronics and quantum computing. But their detection has so far been hindered by the difficulty of calculating topological invariant properties (or topological nodes), which requires both experience with materials and expertise with advanced theoretical tools. Here we introduce an effective, efficient and fully automated algorithm that diagnoses the nontrivial band topology in a large fraction of nonmagnetic materials. Our algorithm is based on recently developed exhaustive mappings between the symmetry representations of occupied bands and topological invariants. We sweep through a total of 39,519 materials available in a crystal database, and find that as many as 8,056 of them are topologically nontrivial. All results are available and searchable in a database with an interactive user interface.**

Symmetry and topology in solids are an entangled pair of concepts in modern physics. Since 2005, theorists<sup>1–3</sup> have been aware that, in the presence of time-reversal symmetry, there are insulators (or nondegenerate ground states with a finite excitation gap in general) that deviate drastically from atomic insulators. These new special insulators host nontrivial topology in their electronic band structures, quantified by a new, global good quantum number—the  $Z_2$  invariant<sup>4,5</sup>. This invariant takes the value of either 0 or 1, and depends on the wavefunctions of the valence bands in the entire Brillouin zone.

Topological insulators, protected by time-reversal symmetry with the  $Z_2$  invariant, were only the first member of an entire family of topological materials to come in the following decade. It is now understood that topological invariants are the defining properties of all topological materials and that they can take different forms, which depend, and depend only, on the dimensionality and the symmetries of the system<sup>6–8</sup>. These symmetries range from on-site symmetries such as time reversal and particle–hole interchange, to spatial symmetries such as translation<sup>3</sup>, reflection<sup>9</sup>, rotation<sup>10–12</sup> and nonsymmorphic symmetries<sup>13,14</sup>, each of which brings new and independent topological invariants. Hence a full characterization of the topology of a given crystal amounts to listing all of the invariants protected by all elements in the corresponding space group.

Parallel to this line of investigation has been the emergence of the field of topological semimetals<sup>15–20</sup>, in which the conduction and the valence bands have band crossings—that is, topological nodes that cannot be removed by symmetry-preserving perturbations. Depending on the degeneracy and dimensionality of their nodes, topological semimetals can be further classified into nodal-point and nodal-line semimetals. A topological semimetal is characterized by the number and the type of all of its band crossings<sup>21</sup>.

Numerical prediction of topological materials thus requires the evaluation of all topological invariants, or the identification of all topological nodes, both of which amount to involved calculations<sup>22</sup>.

The expressions of some topological invariants are highly complicated<sup>13,23,24</sup> for direct evaluation, and some invariants do not even have close-form expressions<sup>10–12</sup>. The challenge has prevented people from carrying out any large-scale, comprehensive search for topological materials, and successful examples have been ascribed mostly to the experience and intuition of researchers.

Following the theory of topological quantum chemistry<sup>25</sup> and that of symmetry-based indicators<sup>26</sup>, a series of recent theoretical works has greatly improved the situation by completely mapping the irreducible representations of valence bands onto topological invariants<sup>27–29</sup> and topological nodes<sup>30</sup>. Recognizing that these theories can be fused together with first-principles numerical methods, we have developed a fully automated search algorithm that can readily be used to scan through large materials databases.

## Algorithm

We now briefly describe the automatic diagnostic process that we have designed for any given nonmagnetic crystal (Fig. 1). Some important technical details needed to reproduce our findings are given in the Methods.

In the preparation phase, we import a material that is simultaneously registered in the online crystal database the Materials Project (<https://materialsproject.org>)<sup>31</sup> and the Inorganic Crystal Structure Database (ICSD; [http://www2.fiz-karlsruhe.de/icsd\\_home.html](http://www2.fiz-karlsruhe.de/icsd_home.html))<sup>32</sup>. If the material has a magnetic moment higher than  $0.1 \mu_B$  per unit cell (according to its Materials Project record), we label it as ‘magnetic’ and stop further analysis, as the theory works for nonmagnetic materials only. Also excluded from further analysis are materials with an odd number of electrons per unit cell, which are labelled as ‘conventional metals’. Otherwise, we proceed to standardize the input crystal structure for the next phase.

In the calculation phase, the imported atomic positions and a certain set of pseudopotentials are first used to obtain the self-consistent electron density using the Vienna ab initio simulation package (VASP)<sup>33</sup>.

<sup>1</sup>Beijing National Laboratory for Condensed Matter Physics and Institute of Physics, Chinese Academy of Sciences, Beijing, China. <sup>2</sup>University of Chinese Academy of Sciences, Beijing, China.

<sup>3</sup>Computer Network Information Center, Chinese Academy of Sciences, Beijing, China. <sup>4</sup>Kavli Institute for Theoretical Sciences, Chinese Academy of Sciences, Beijing, China. <sup>5</sup>Collaborative Innovation Center of Quantum Matter, Beijing, China. <sup>6</sup>Songshan Lake Materials Laboratory, Dongguan, China. <sup>7</sup>CAS Centre for Excellence in Topological Quantum Computation, Beijing, China.

<sup>8</sup>Physical Science Laboratory, Huairou National Comprehensive Science Center, Beijing, China. <sup>9</sup>These authors contributed equally: Tiantian Zhang, Yi Jiang, Zhida Song. \*e-mail: hmweng@iphy.ac.cn; cfang@iphy.ac.cn

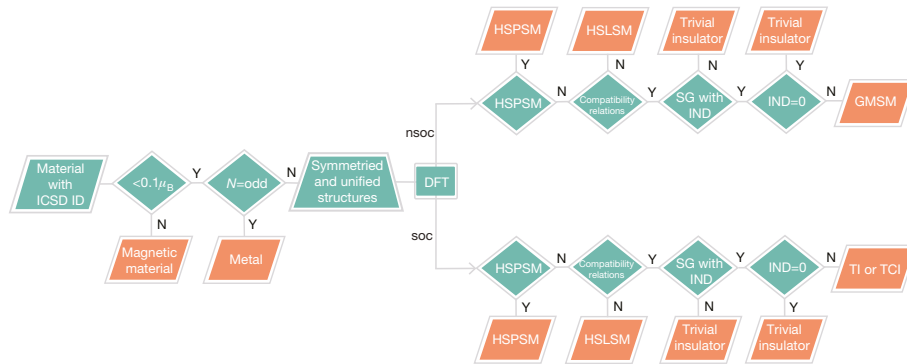


**Fig. 1 | Flow chart for our automatic diagnostic algorithm.** For a given material found in the ICSD and the Materials Project, we first check against the record at the Materials Project to see whether it is nonmagnetic (that is, does it have a magnetic moment less than  $0.1 \mu_B$  per unit cell), and whether there is an even number of electrons in one primitive unit cell. If yes for both, we feed the material into a density-functional-theory (DFT) calculation of the band structure and compute symmetry data, before checking whether there are partially filled irreducible representations at high-symmetry points. If not, the symmetry data are checked against all

Once the density converges, it is used to compute the energy levels and wavefunctions at a given list of high-symmetry points in the Brillouin zone. At each high-symmetry point, we rank the energy levels from low to high, and we define the first  $N$  bands as the valence bands (Fig. 2), where  $N$  is the number of electrons per unit cell. (Note that this working definition deviates from the conventional notion of valence bands.) We store the wavefunctions of all occupied bands at high-symmetry points for the next phase.

In the analysis phase, using a script in conjunction with the data on the Bilbao Crystallographic Server<sup>34</sup>, we identify the irreducible representation for each (multiplet of) valence band(s). Then, from this, another script is used to check whether there is band touching or crossing between the  $N$ th and the  $N+1$ -th band at any high-symmetry point or along any high-symmetry line, the latter of which requires an exhaustive list of compatibility relations, also available on the Bilbao Crystallographic Server thanks to recent efforts<sup>25,34</sup>. A material that has degeneracy at high-symmetry points or high-symmetry lines is labelled as high-symmetry-point semimetal (HSPSM) or high-symmetry-line semimetal (HLSLM), respectively. For a band structure that does not have such degeneracy, we proceed to compute all of its symmetry-based indicators. Symmetry-based indicators<sup>26</sup> directly inform whether the material is a topological insulator, a topological crystalline insulator (TCI) or a topological semimetal, and give all possible sets of the topological invariants<sup>27,28</sup> or topological nodes<sup>30</sup>. From the values of the indicators, the material can be labelled as generic-momenta semimetal (GMSM, having topological nodes at non-high-symmetry momenta), topological insulator or TCI. This concludes the final phase of the algorithm.

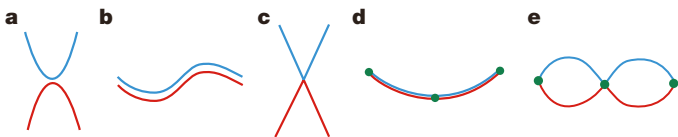


**Fig. 2 | Definition of valence bands and conduction bands.** The red band represents the top valence and the blue the bottom conduction band, for the following cases: **a**, insulator or semiconductor; **b**, compensation semimetal; **c**, topological semimetal; **d**, metal with an odd number of electrons per unit cell on a centrosymmetric lattice; and **e**, metal with an odd number of electrons per unit cell on a noncentrosymmetric lattice. The green dots in **d**, **e** represent Kramer's degeneracy owing to time-reversal symmetry. Note that our definitions for **d**, **e** differ from conventional definitions.

compatibility relations, and, should all relations be satisfied, the data are fed into the calculation of symmetry-based indicators. At each checkpoint, a material either goes on to the next step, or is labelled as magnetic, conventional metal, high-symmetry point semimetal or high-symmetry line semimetal. At the final step, depending on the values of indicators, a material is labelled as GMSM, TI, TCI or insulator with trivial indicators. At the first-principles calculation step and all following steps, two possible settings are applied to all steps: nsoc or soc. DFT, density functional theory; IND, symmetry-based indicator(s); SG, space group.

### Identification of five topological classes

We have run the above algorithm through a total of 39,519 crystals, of which we find 10,348 to be magnetic, and 2,483 to be conventional metals. We carried out first-principles calculations for 26,522 materials, from which we detect 8,056 topological materials in the presence of spin-orbit coupling, sorted into 2,713 HSPSMs, 2,292 HLSLMs, 1,814 topological insulators and 1,237 TCIs.

In electronic systems, the spin-orbit coupling is always finite, but there are materials consisting of light atoms that have negligible spin-orbit coupling—that is, the spin-orbit coupling is much smaller compared with other energy scales such as the Fermi energy or temperature. For these materials, diagnosing the topology while assuming an absence of spin-orbit coupling is physically more relevant. For example, identifying graphene as a Dirac semimetal is more relevant than declaring it to be a topological insulator with a gap of roughly  $10^{-6}$  eV. Because of this, for each material, we carry out the calculation and analysis twice—once with spin-orbit coupling ('soc setting') and once without ('nsoc setting'). When using the nsoc setting, materials that have band degeneracy between the valence and conduction bands at high-symmetry points and along high-symmetry lines are also sorted as HSPSM and HLSLM, respectively. If the band structure does not have any such degeneracy, we proceed to calculate the symmetry-based indicators. In the absence of spin-orbit coupling, all indicators correspond to topological nodes at non-high-symmetry momenta<sup>30</sup>, and therefore materials that have non-zero indicators are all GMSMs. The type and configuration of the topological nodes for each non-zero set of indicators are found in ref.<sup>30</sup>. For the nsoc setting, we find 8,889 materials to be topological, classified as 5,508 HSPSMs, 3,269 HLSLMs and 112 GMSMs.

Each material is now labelled with one of the following: HSPSM, high-symmetry point semimetal (both settings); HLSLM, high-symmetry line semimetal (both settings); GMSM, generic-momenta semimetal (nsoc setting only); TI, topological insulator (soc setting only); TCI, topological crystalline insulator (soc setting only); magnetic; conventional metal; or insulator with trivial indicators. Out of these, we consider the first five classes to be topological materials; we list the materials according to their class in Supplementary Tables I–V. In Supplementary Table I, each HSPSM material is shown together with high-symmetry points at which partial fillings occur, and irreducible representations that are partially filled. Each HLSLM material in Supplementary Table II is shown together with the high-symmetry line(s) at which band crossings between the  $N$ th and the  $N+1$ -th bands appear. Each GMSM, TI and TCI material—listed in Supplementary Tables III, IV and V respectively—is shown together with the values of its symmetry-based indicators.

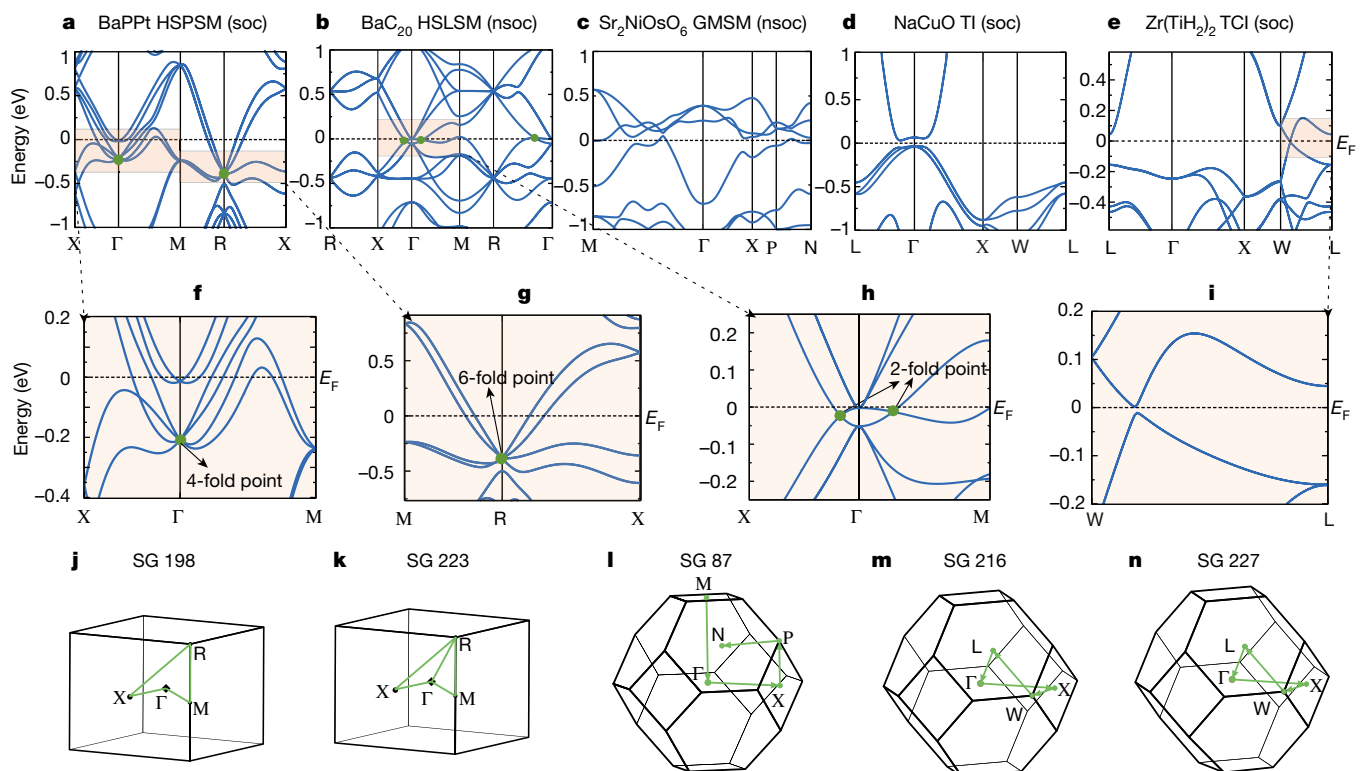


**Fig. 3 | The five candidates for the five classes of topological material.** **a, f, g, j,** The HSPSM BaPpt, which has sixfold degeneracy near the Fermi energy at R. **b, h, k,** The HSLSM BaC<sub>20</sub>, which has negligible spin-orbit coupling and nine connected nodal rings centred at  $\Gamma$ . **c, l,** The GMSM Sr<sub>2</sub>NiOsO<sub>6</sub>, with nodal rings that have Z<sub>2</sub>-monopole charge (nsoc setting).

**d, m,** The topological insulator NaCuO. **e, i, n,** The TCI Zr(TiH<sub>2</sub>)<sub>2</sub>. For each candidate material, we plot the band structure in **a–e**, the Brillouin zone with high-symmetry points in **j–n**, and if necessary, zoomed-in regions of the band structure **f–i**.

Our extensive sweep of materials includes a large fraction of all crystals ever synthesized, and we detect nontrivial topology in about 30% of the 26,522 calculated nonmagnetic materials. This abundance of topological materials overturns the sentiment of many, including us, that they are special and rare in nature. Without any tuning parameter or human intervention, these many materials from the sweep include almost all topological materials known so far, such as bismuth selenide (Bi<sub>2</sub>Se<sub>3</sub>), a topological insulator; tin telluride (SnTe), a TCI; and sodium bismuthide (Na<sub>3</sub>Bi), a topological semimetal. More importantly, this catalogue includes materials for which the nontrivial topology was previously unknown.

### Representative materials from the five topological classes

Below we choose one candidate from each class for discussion. Out of the five, four have not, to the best of our knowledge, been discussed previously in the literature, and four host new topological invariants or topological nodes that have not been experimentally discovered in real materials. We find barium phosphorus platinum (BaPpt; Fig. 3a)<sup>35,36</sup> to be a HSPSM, in which the conduction and the valence bands meet at the high-symmetry points  $\Gamma$  and R. The degeneracy at R is sixfold-stabilized by nonsymmorphic space-group symmetries, and importantly there is an electron pocket near R. These facts qualify BaPpt (soc setting) as a good candidate for the study of topological nodes beyond Weyl and Dirac nodes in real materials<sup>37</sup>.

From the HSLSM class, we highlight cubic barium fullerene (BaC<sub>20</sub>; Fig. 3b; nsoc setting), from space group 223; this material has one fullerene and three barium atoms per unit cell. The violation of compatibility relations along  $\Gamma$ -X,  $\Gamma$ -M and  $\Gamma$ -R indicates band crossings along these three lines and their symmetry partners. Further analysis (see Methods) shows that these crossing points are parts of the nine interconnected nodal rings that are centred at  $\Gamma$ .

The osmium double perovskite Sr<sub>2</sub>NiOsO<sub>6</sub> (Fig. 3c; nsoc setting), a GMSM, does not have any band crossings along any of the

high-symmetry lines, but the symmetry indicators of (0002) imply that at generic momenta there must be 2-mod-4 nodal rings where the conduction and the valence bands cross. Each of the rings has Z<sub>2</sub>-topological charge<sup>38</sup>, making Sr<sub>2</sub>NiOsO<sub>6</sub> the first candidate electronic material (with small spin-orbit coupling) that hosts Z<sub>2</sub>-nontrivial nodal rings.

Sodium oxocuprate (NaCuO; soc setting) is a new noncentrosymmetric topological insulator (Fig. 3d), having three band inversions between the *d*-orbital and the *s*-orbital at  $\Gamma$ , with an inverted bandgap of about 0.1 eV. For noncentrosymmetric systems, the classical Fu–Kane formula<sup>39</sup> does not apply, so an eigenvalue diagnosis would be impossible without our new method.

Finally, zirconium titanium hydride (Zr(TiH<sub>2</sub>)<sub>2</sub>; Fig. 3e) has band crossings along L–W without spin-orbit coupling, but as the coupling turns on it opens a full gap of about 10 meV at all momenta, making the material a TCI. The symmetry indicators of (0002) pin down the topological invariants of this TCI to two possible sets. Our method cannot distinguish them further, but a calculation of the mirror Chern number at the  $k_z = 0$  plane helps us to choose the correct set (see Methods). In this set, all non-zero invariants are protected by screw-rotation symmetries or glide-plane symmetries, so that Zr(TiH<sub>2</sub>)<sub>2</sub> is a materials candidate for a screw-axis Z<sub>2</sub> TCI, having one-dimensional helical edge states on its surface without two-dimensional surface states for certain sample configurations (see Methods for details). Such TCIs are also known as second-order topological insulators<sup>40–42</sup>.

The entire catalogue is available at <http://materiae.iphy.ac.cn/>, which has an interactive user interface that facilitates searching of the vast amount of data. It also shows the band structures and density of states for each material diagnosed as topological.

### Discussion

Although the abundance of topological materials in nature is good news, the immediate difficulty is that we do not have a simple way

of ranking these many candidates, because there is no universal standard for an ideal topological material. Sometimes it is one that has a topological bandgap or topological Fermi surface that does not coexist with trivial pockets of carriers; but sometimes we particularly look for the presence and interplay of the latter (for example in the case of the recently discovered topological superconductivity in iron selenide, FeSe<sup>43–45</sup>). Some people are interested in three-dimensional topological states<sup>46</sup>; but quasi-two-dimensional topological materials are also desirable for good reasons<sup>47</sup>. Some want the coexistence of band topology and ferroelectricity<sup>48</sup>, and some are looking for a high receptibility to magnetic or superconducting dopants<sup>49</sup>. We have adopted a relatively traditional standard in the field of topological materials: that better topological gapped materials have larger energy gaps (for topological insulators and TCIs), and better topological gapless materials have a lower density of states (for HSPSMs, HSLSMs and GMSMs), with the caveat that the criterion of low density of states does not apply to nodal-line semimetals in general. For each material in the catalogue, we have computed the density of states versus energy, from which we have extracted the energy gap (if any) and the density of states at the Fermi energy. On the basis of these two pieces of data, we have ranked the materials from each class for every space group, using || to separate materials that are better by this standard from the rest (see Supplementary Information). We emphasize that our ranking should only be considered as a reference, and we suggest that readers interested in a particular candidate material should eye-inspect the band structure shown in our online database.

The main outcome of our work is the sorting of nonmagnetic materials into topological classes; we did not aim to find the ‘best’ topological materials. However, it is natural to ask how we would compare the materials found in this exhaustive, sweeping search with those found previously in an ad hoc fashion. We note that, as almost all previously known topological materials have already been included in the catalogue, we can only compare the known materials with the new members in each class. A simple comparison reveals that the newly found materials are not substantially better than the known ones, as judged by our standard of a large gap or smaller density of states. The previously known bismuth selenide (Bi<sub>2</sub>Se<sub>3</sub>) is still the best candidate for a topological insulator in the catalogue, having a gap of around 0.31 eV—larger than the roughly 0.16-eV gap in the best new candidate, strontium lead telluride (Sr<sub>2</sub>Te<sub>4</sub>Pb). The most studied TCI is SnTe, with a gap of 0.188 eV, larger than the 0.072-eV gap of the new candidate Yb<sub>3</sub>PbO (an ytterbium perovskite). The best HSLSM in the literature is probably Na<sub>3</sub>Bi, with space group 194; among the newly discovered materials, the best such material is probably indium antimonide (InSb), with space group 186. The two materials both have Dirac points along  $\Gamma$ -A and a vanishing density of states.

Our method has demonstrated its power in showing the abundance of nontrivial topology that nature has to offer. However, it is equally, if not more, important to expound on the limitations of the method, and to offer caveats to users of the catalogue, which we summarize as follows.

First, the entire theoretical framework of our diagnosis is based on the assumption that valence electrons can be characterized by the physical picture of band theory. However, this assumption breaks down in the presence of strong electron correlation. For this reason, we cannot hope to include any strongly interacting symmetry-protected topological states<sup>50</sup> that have been theoretically proposed, such as the Haldane chain<sup>51</sup>.

Second, we have used first-principles simulations to calculate band structures without any corrections ascribed to electron correlation, for the latter require additional artificial parameters. For this reason, band structures of materials consisting of *d*- and *f*-electrons<sup>52,53</sup> near the Fermi energy may be incorrect. Thus, in Supplementary Tables I–V, certain elements that are known to host partially filled *d*- or *f*-electrons in compounds are marked with blue or red, respectively. Users should be aware that the first-principles calculation has a tendency to overestimate the inverted bandgap.

Third, our method—or indeed any eigenvalue diagnosis method—takes as inputs only those symmetry data that are found at certain high-symmetry points, and therefore cannot detect band inversions away from these points. This is the origin of the one-to-many nature of the mappings from symmetry-based indicators to topological invariants<sup>27,28</sup> or nodes<sup>30</sup>. Physically, it means that if some nontrivial topology derives from band inversions away from any high-symmetry point, the diagnosis would not detect it, instead identifying the material as trivial. This leads to the absence of the famous Weyl semimetal tantalum arsenide (TaAs) from the catalogue. TaAs<sup>54,55</sup> has band inversions at  $\Sigma$  and S, neither of which is a high-symmetry point.

Fourth, our method assumes the nonmagnetic state of a material when diagnosing topology, but cannot diagnose magnetism itself. The magnetic moment listed on the Materials Project website has been calculated using a first-principles simulation with an additional parameter, Hubbard U, and a ferromagnetic initial state. This simple numerical diagnosis is not supposed to capture any type of antiferromagnetism, and may also misidentify some ferromagnetism as nonmagnetism (and vice versa). We suggest that readers interested in a particular material should check for possible magnetism in the experimental literature.

Fifth, in some materials—such as bismuth bromide (Bi<sub>4</sub>Br<sub>4</sub>) and lithium silver antimonide (Li<sub>2</sub>AgSb)—the ordering of bands near the Fermi energy depends critically on the lattice constants or the choice of pseudopotential. As a rule, we have used the experimental lattice parameters without relaxation. But if the gap in a material is very small, we would suggest doing the calculation again with slightly different input parameters (such as relaxed lattice constants) to see whether the result is stable.

Finally, conventional metals can in principle also be called HSPSMs, because at each of the eight time-reversal invariant momenta, the *N*th and the *N*+1-th bands necessarily touch owing to Kramer’s degeneracy. However, these materials usually have trivial carrier pockets that are far larger than the topological ones, and we therefore exclude them from our list of topological materials.

## Conclusion

We have designed an algorithm for quickly diagnosing nontrivial topology in nonmagnetic materials, using only the symmetry data from high-symmetry points in the Brillouin zone as inputs. We have applied the algorithm to all materials registered in the Materials Project and the ICSD. Contrary to popular thinking that nontrivial topology is exotic and scarce, we have found that more than 30% (8,056 out of 26,688) of the studied materials are topological.

## Online content

Any methods, additional references, Nature Research reporting summaries, source data, statements of data availability and associated accession codes are available at <https://doi.org/10.1038/s41586-019-0944-6>.

Received: 5 July 2018; Accepted: 19 December 2018;  
Published online 27 February 2019.

1. Kane, C. L. & Mele, E. J. Z<sub>2</sub> topological order and the quantum spin Hall effect. *Phys. Rev. Lett.* **95**, 146802 (2005).
2. Bernevig, B. A., Hughes, T. L. & Zhang, S. C. Quantum spin Hall effect and topological phase transition in HgTe quantum wells. *Science* **314**, 1757–1761 (2006).
3. Fu, L., Kane, C. L. & Mele, E. J. Topological insulators in three dimensions. *Phys. Rev. Lett.* **98**, 106803 (2007).
4. Hasan, M. Z. & Kane, C. L. Colloquium: topological insulators. *Rev. Mod. Phys.* **82**, 3045 (2010).
5. Qi, X. L. & Zhang, S. C. Topological insulators and superconductors. *Rev. Mod. Phys.* **83**, 1057 (2011).
6. Schnyder, A. P., Ryu, S., Furusaki, A. & Ludwig, A. W. Classification of topological insulators and superconductors in three spatial dimensions. *Phys. Rev. B* **78**, 195125 (2008).
7. Kitaev, A. Periodic table for topological insulators and superconductors. *AIP Conf. Proc.* **1134**, 22–30 (2009).
8. Chiu, C. K., Teo, J. C., Schnyder, A. P. & Ryu, S. Classification of topological quantum matter with symmetries. *Rev. Mod. Phys.* **88**, 035005 (2016).
9. Hsieh, T. H. et al. Topological crystalline insulators in the SnTe material class. *Nat. Commun.* **3**, 982 (2012); corrigendum 4, 1901 (2013).

10. Song, Z., Fang, Z. & Fang, C. ( $d-2$ )-dimensional edge states of rotation symmetry protected topological states. *Phys. Rev. Lett.* **119**, 246402 (2017).
11. Fang, C. & Fu, L. Rotation anomaly and topological crystalline insulators. Preprint at <https://arxiv.org/abs/1709.01929> (2017).
12. Schindler, F. et al. Higher-order topological insulators. *Sci. Adv.* **4**, eaat0346 (2018).
13. Wang, Z., Alexandradinata, A., Cava, R. J. & Bernevig, B. A. Hourglass fermions. *Nature* **532**, 189–194 (2016).
14. Wieder, B. J. et al. Wallpaper fermions and the nonsymmorphic Dirac insulator. *Science* **361**, 246–251 (2018).
15. Fang, Z. et al. The anomalous Hall effect and magnetic monopoles in momentum space. *Science* **302**, 92–95 (2003).
16. Murakami, S. Phase transition between the quantum spin Hall and insulator phases in 3D: emergence of a topological gapless phase. *New J. Phys.* **9**, 356 (2007); corrigendum **10**, 029802 (2008).
17. Wan, X., Turner, A. M., Vishwanath, A. & Savrasov, S. Y. Topological semimetal and Fermi-arc surface states in the electronic structure of pyrochlore iridates. *Phys. Rev. B* **83**, 205101 (2011).
18. Young, S. M. et al. Dirac semimetal in three dimensions. *Phys. Rev. Lett.* **108**, 140405 (2012).
19. Wang, Z. et al. Dirac semimetal and topological phase transitions in  $A_3Bi$  ( $A = Na, K, Rb$ ). *Phys. Rev. B* **85**, 195320 (2012).
20. Burkov, A. A., Hook, M. D. & Balents, L. Topological nodal semimetals. *Phys. Rev. B* **84**, 235126 (2011).
21. Armitage, N. P., Mele, E. J. & Vishwanath, A. Weyl and Dirac semimetals in three-dimensional solids. *Rev. Mod. Phys.* **90**, 015001 (2018).
22. Yu, R., Qi, X. L., Bernevig, A., Fang, Z. & Dai, X. Equivalent expression of  $Z_2$  topological invariant for band insulators using the non-abelian Berry connection. *Phys. Rev. B* **84**, 075119 (2011).
23. Fang, C. & Fu, L. New classes of three-dimensional topological crystalline insulators: nonsymmorphic and magnetic. *Phys. Rev. B* **91**, 161105 (2015).
24. Shiozaki, K., Sato, M. & Gomi, K.  $Z_2$  topology in nonsymmorphic crystalline insulators: Möbius twist in surface states. *Phys. Rev. B* **91**, 155120 (2015).
25. Bradlyn, B. et al. Topological quantum chemistry. *Nature* **547**, 298–305 (2017).
26. Po, H. C., Vishwanath, A. & Watanabe, H. Symmetry-based indicators of band topology in the 230 space groups. *Nat. Commun.* **8**, 50 (2017); erratum **8**, 931 (2017).
27. Song, Z., Zhang, T., Fang, Z. & Fang, C. Quantitative mappings between symmetry and topology in solids. *Nat. Commun.* **9**, 3530 (2018).
28. Khalaf, E., Po, H. C., Vishwanath, A. & Watanabe, H. Symmetry indicators and anomalous surface states of topological crystalline insulators. *Phys. Rev. X* **8**, 031070 (2018).
29. Kruthoff, J., de Boer, J., van Wezel, J., Kane, C. L. & Slager, R. J. Topological classification of crystalline insulators through band structure combinatorics. *Phys. Rev. X* **7**, 041069 (2017).
30. Song, Z., Zhang, T. & Fang, C. Diagnosis for nonmagnetic topological semimetals in the absence of spin-orbital coupling. *Phys. Rev. X* **8**, 031069 (2018).
31. Jain, A. et al. Commentary: the materials project: a materials genome approach to accelerating materials innovation. *APL Mater.* **1**, 011002 (2013).
32. Hellenbrandt, M. The inorganic crystal structure database (ICSD)—present and future. *Crystallogr. Rev.* **10**, 17–22 (2004).
33. Kresse, G. & Furthmüller, J. Efficient iterative schemes for ab initio total-energy calculations using a plane-wave basis set. *Phys. Rev. B* **54**, 11169 (1996).
34. Elcoro, L. et al. Double crystallographic groups and their representations on the Bilbao Crystallographic Server. *J. Appl. Cryst.* **50**, 1457–1477 (2017).
35. Chang, G. et al. Unconventional chiral fermions and large topological Fermi arcs in RhSi. *Phys. Rev. Lett.* **119**, 206401 (2017).
36. Flicker, F. et al. Chiral optical response of multifold fermions. *Phys. Rev. B* **98**, 155145 (2018).
37. Bradlyn, B. et al. Beyond Dirac and Weyl fermions: unconventional quasiparticles in conventional crystals. *Science* **353**, aaf5037 (2016).
38. Fang, C., Chen, Y., Kee, H. Y. & Fu, L. Topological nodal line semimetals with and without spin-orbital coupling. *Phys. Rev. B* **92**, 081201 (2015).
39. Fu, L. & Kane, C. L. Topological insulators with inversion symmetry. *Phys. Rev. B* **76**, 045302 (2007).
40. Benalcazar, W. A., Bernevig, B. A. & Hughes, T. L. Quantized electric multipole insulators. *Science* **357**, 61–66 (2017).
41. Langbehn, J., Peng, Y., Trifunovic, L., von Oppen, F. & Brouwer, P. W. Reflection-symmetric second-order topological insulators and superconductors. *Phys. Rev. Lett.* **119**, 246401 (2017).
42. Benalcazar, W. A., Bernevig, B. A. & Hughes, T. L. Electric multipole moments, topological multipole moment pumping, and chiral hinge states in crystalline insulators. *Phys. Rev. B* **96**, 245115 (2017).
43. Zhang, P. et al. Observation of topological superconductivity on the surface of an iron-based superconductor. *Science* **360**, 182–186 (2018).
44. Wang, D. et al. Evidence for Majorana bound states in an iron-based superconductor. *Science* **362**, 333–335 (2018).
45. Yin, J. X. et al. Observation of a robust zero-energy bound state in iron-based superconductor Fe (Te, Se). *Nat. Phys.* **11**, 543–546 (2015).
46. Zhang, H. et al. Topological insulators in  $Bi_2Se_3$ ,  $Bi_2Te_3$  and  $Sb_2Te_3$  with a single Dirac cone on the surface. *Nat. Phys.* **5**, 438–442 (2009).
47. Qian, X., Liu, J., Fu, L. & Li, J. Quantum spin Hall effect in two-dimensional transition metal dichalcogenides. *Science* **346**, 1344–1347 (2014).
48. Chang, K. et al. Discovery of robust in-plane ferroelectricity in atomic-thick SnTe. *Science* **353**, 274–278 (2016).
49. Chang, C. Z. et al. Experimental observation of the quantum anomalous Hall effect in a magnetic topological insulator. *Science* **340**, 167–170 (2013).
50. Gu, Z. C. & Wen, X. G. Tensor-entanglement-filtering renormalization approach and symmetry-protected topological order. *Phys. Rev. B* **80**, 155131 (2009).
51. Affleck, I. Quantum spin chains and the Haldane gap. *J. Phys. Condens. Matter* **1**, 3047 (1989).
52. Dzero, M., Sun, K., Galitski, V. & Coleman, P. Topological kondo insulators. *Phys. Rev. Lett.* **104**, 106408 (2010).
53. Lu, F., Zhao, J., Weng, H., Fang, Z. & Dai, X. Correlated topological insulators with mixed valence. *Phys. Rev. Lett.* **110**, 096401 (2013).
54. Weng, H., Fang, C., Fang, Z., Bernevig, B. A. & Dai, X. Weyl semimetal phase in noncentrosymmetric transition-metal monophosphides. *Phys. Rev. X* **5**, 011029 (2015).
55. Huang, S. M. et al. A Weyl Fermion semimetal with surface Fermi arcs in the transition metal monophosphide TaAs class. *Nat. Commun.* **6**, 7373 (2015).

**Acknowledgements** We are grateful for suggestions and comments from M. Liu, B. Bradlyn, H. Watanabe and B. Wieder. We acknowledge support from the Ministry of Science and Technology of China under grant numbers 2016YFA0302400, 2016YFA0300600 and 2018YFA0305700; the National Science Foundation of China under grant numbers 11674370, 11421092 and 11674369; and the Chinese Academy of Sciences under grant numbers XXH13506-202, XDB07020100 and XDB28000000. We also acknowledge support from the Science Challenge Project (number TZ2016004), the K. C. Wong Education Foundation (GJTD-2018-01), the Beijing Municipal Science and Technology Commission (Z181100004218001) and the Beijing Natural Science Foundation (Z180008).

**Reviewer information** Nature thanks J. Checkelsky, M. Franz and the other anonymous reviewer(s) for their contribution to the peer review of this work.

**Author contributions** C.F. conceived the work; H.W. and Z.F. were in charge of the numerical methods and checked for consistency with previous works; T.Z. did the major part of the calculations and analyses of materials; Y.J., Z.S., H.H. and Y.H. wrote the code for analysing irreducible representations and symmetry-based indicators; H.H. and Y.H. built the website. C.F., H.W. and Z.F. wrote the main text; and T.Z., Y.J. and Z.S. wrote the Methods section and the Supplementary Information.

**Competing interests** The authors declare no competing interests.

#### Additional information

**Extended data** is available for this paper at <https://doi.org/10.1038/s41586-019-0944-6>.

**Supplementary information** is available for this paper at <https://doi.org/10.1038/s41586-019-0944-6>.

**Reprints and permissions information** is available at <http://www.nature.com/reprints>.

**Correspondence and requests for materials** should be addressed to H.W. or C.F. **Publisher's note:** Springer Nature remains neutral with regard to jurisdictional claims in published maps and institutional affiliations.

© The Author(s), under exclusive licence to Springer Nature Limited 2019

## METHODS

**Choice of input crystal data.** Crystal data—including space-group numbers, lattice parameters ( $a, b, c, \alpha, \beta, \gamma$ ) and atomic positions—are imported from the experimental values recorded in the Materials Project<sup>31,56</sup>. To the best of our knowledge, the Materials Project collects experimental crystal data from the ICSD<sup>32</sup> and reorganizes them. The ICSD has duplicated entries; to handle this, the Materials Project identifies two materials as the same if their lattice parameters and atomic positions differ by values less than a given threshold. The Materials Project also has a requirement for the accuracy of atomic positions, so that if the position of any atom cannot be experimentally determined up to a preset error, the corresponding material would not be added to the Materials Project. Taking into account duplicates and data accuracy, the 199,466 records in ICSD become 39,519 records in the Materials Project.

The Materials Project is a database of materials with their properties obtained from standardized numerical simulations. One of the properties is magnetism, which is given in terms of the total magnetic moment per unit cell, in units of  $\mu_B$ . This value is obtained from a density functional theory (DFT) calculation or a DFT + U calculation, with a ferromagnetic initial state of the electrons. We comment that a more reliable way of determining potential magnetism is to use various possible magnetic structures in the initial state, and to compare the convergent energies, identifying the lowest energy state as the ground state. However, it is unclear how one could reasonably enumerate all candidate magnetic structures, so the diagnosis for magnetism is generally considered difficult. We note that for several materials, the calculated magnetic moment differs from experimental data. For example,  $\text{MnAlCo}_2$  and  $\text{Fe}_5\text{Si}_3$  have been found to be ferromagnetic at lower temperatures, yet they show negligible magnetic moments in their Materials Project records. We note that antiferromagnetism is not thought to be captured by the numerical simulations either.

Band topology is mostly stable against small perturbations in the lattice parameters. Yet there are certain materials for which the gaps are so close to the inversion point that a small change in lattice parameters leads to a transition from nontopological to topological and vice versa. For example, for  $\text{Ca}_3\text{NBi}$  and  $\text{TlBiSe}_2$ , results of the topological diagnosis depend on whether the experimental value or the calculated value of the lattice constants is used. Here, the calculated value refers to the value after a simulated relaxation of the lattice, optimizing the total energy.

In addition, before feeding the crystal data to the DFT calculation, we check the consistency between the atomic positions and the space group. We find 166 materials that do not pass the consistency test within an error of up to 0.1 Å, and exclude them from further processing.

**Band topology in conventional metals.** Materials that have an odd number of electrons per unit cell are labelled as conventional metals and excluded from further diagnosis. The reason is simple: all these materials should be classified as HSPSMs, so analysis becomes unnecessary. This is because all bands are at least doubly degenerate at time-reversal momenta owing to Kramer's degeneracy. Any odd number filling then necessarily leads to partial filling at every time-reversal momentum, making the material a HSPSM.

We note that further classification among these metals, which we do not perform here, amounts to determining the dimension of the band crossing. For example, if there is inversion symmetry, then time reversal and inversion jointly protect double degeneracy at every momentum in the Brillouin zone: this is three-dimensional crossing. In the presence of a twofold screw axis, this symmetry together with time reversal lead to double degeneracy at an entire high-symmetry plane, which is a two-dimensional crossing at the boundary of the Brillouin zone. In the presence of a glide plane, this symmetry together with time reversal lead to double degeneracy along certain lines at the boundary of the Brillouin zone, and this crossing is one dimensional. If none of screw axis, glide plane or inversion is present, the bands are generally nondegenerate at any momentum away from a time-reversal invariant momentum, so that these momenta are discrete Weyl points—that is, zero-dimensional crossings.

**Settings for the first-principles calculation.** All of the calculations herein are performed by VASP<sup>33,57–59</sup> with the generalized gradient approximation (GGA) of the Perdew–Burke–Ernzerhof (PBE)-type exchange–correlation potential. The pseudopotential files that we used are from the VASP software package and are listed at <http://materials.iphys.ac.cn/>. The cut-off energy of the plane wave basis set is set to be the ENMAX value in the pseudopotential file plus 25%. A  $\Gamma$ -centred Monkhorst–Pack grid with 30  $k$ -points per Å<sup>-1</sup> is used for the self-consistent calculations. A maximum number of electronic self-consistency steps is given in our calculations, such that a material for which the calculation does not converge within 300 self-consistency loop steps is labelled and discarded. Two itinerant schemes are used in this process: the special Davidson block iteration scheme, and residual minimization method direct inversion in the iterative subspace (RMM-DIIS). About 400 materials are not converged or converge to wrong states in the nsoc setting, and 600 in the soc-setting.

While the mapping from symmetry data to topology data is mathematically rigorous, the validity of GGA depends on the actual material: if a material has a significant correlation effect at the Fermi energy, the results are likely to be inaccurate. For example, for compounds containing rare-earth elements with possibly partial-filling  $f$ -orbitals, the strong correlation effect is dominant; we have left these materials for further detailed study. From experience, in Supplementary Tables I–V we have highlighted a few elements that often induce strong correlation effects in compounds owing to partially filled  $d$ - or  $f$ -shells (blue for  $d$  and red for  $f$ ). We have not highlighted titanium, yttrium, zirconium, niobium, molybdenum, lanthanum, lutetium, hafnium, tantalum, tungsten and platinum because, although they have partially filled  $d$ -shells, in many known cases they do not bring about strong correlation effects.

The original data loaded from the Materials Project are not in a unified convention; for example, the orientation of the primitive cell is arbitrary, as is the choice of origin point. In order to implement automated high-throughput calculations and to ensure that VASP can find the right symmetry, we symmetrize and standardize the atomic positions using PHONOPY<sup>60</sup> after loading the lattice parameters and atomic positions. At this step, we discarded 166 materials for discrepancy in the space groups identified in PHONOPY and those given in the databases, up to an error tolerance of 0.1 Å in atomic position.

**Extracting irreducible representations.** The irreducible representation for each group of degenerate valence bands is obtained by calculating the character of each symmetry operation and looking up the character tables on the Bilbao Crystallographic Server. To be specific, first the plane wave expansion coefficients of wavefunctions are read from the VASP output file, and then, by applying different space-group symmetry operations to the wavefunctions, we obtain the corresponding character. Attention needs to be paid in the choice of convention in symmetry operations, including the coordinate origin and orientation, as well as the spin rotation axis of the SU(2) part of the symmetry operation. In determining the presence of degeneracy, we use an energy error of  $\min(0.5 \text{ meV}, 0.1 \Delta_k)$ , where  $\Delta_k$  is the gap between valence bands and conduction bands at the  $k$ -point) to avoid possible numerical level splitting from VASP. Failing to find irreducible representations formed by ‘degenerate’ bands identified in this way implies a low quality of convergence. In such cases we improve the convergence threshold and redo the self-consistent and non-self-consistent calculations until we can successfully identify each group of degenerate bands with a certain irreducible representation.

**Nodal lines in  $\text{BaC}_{20}$ .** Using the nsoc setting, we identify  $\text{BaC}_{20}$  (space group 223) as an HSLSM, the band structure of which breaks compatibility relations along  $\Gamma$ -X,  $\Gamma$ -M and  $\Gamma$ -R. Below we show that these crossings are intersections of nine nodal rings with high symmetry lines in the Brillouin zone, wherein three of the rings lie in the  $k_i = 0$  ( $i = x, y, z$ ) planes and six lie in the  $k_i \pm k_j = 0$  ( $i, j = x, y, z, i \neq j$ ) planes. The  $k_i = 0$  rings can be diagnosed from the crossings along  $\Gamma$ -X and  $\Gamma$ -M, both of which interchange a valence band having a mirror ( $\{m_{001}|0\}$ ) eigenvalue of  $-1$  with a conduction band with a mirror eigenvalue of  $+1$ . Because of these crossings, the valence bands at  $\Gamma$  have one more (or less)  $-1$  (or  $+1$ ) mirror eigenvalue than the valence bands at X or M, implying nodal ring(s) protected by the mirror symmetry in the  $k_z = 0$  plane. Such mirror eigenvalues at  $\Gamma$ , X and M allow a few possible configurations of the ring(s). For example, there may be a single ring surrounding  $\Gamma$ ; or there may be a single ring surrounding X, a single ring surrounding Y (that is, the  $C_3$  ( $\{3_{111}|000\}$ ) partner of X in the  $k_y$  axis) and a single ring surrounding M; and so on. Further band-structure calculation shows that  $\text{BaC}_{20}$  belongs to the first case, that is, it has a single ring surrounding  $\Gamma$  in the  $k_z = 0$  plane. Owing to the  $C_3$  rotation symmetry, there are in total three nodal rings in the  $k_i = 0$  planes (Extended Data Fig. 1a). The  $k_i \pm k_j = 0$  rings can be diagnosed in a similar way: the crossings along the  $\Gamma$ -M and  $\Gamma$ -R interchange a valence band having a glide ( $\{m_{1\bar{1}0}|\frac{1}{2}\frac{1}{2}\frac{1}{2}\}$ ) eigenvalue  $e^{-i\pi k/2}$  with a conduction band having a glide eigenvalue  $-e^{-i\pi k/2}$ , where  $\mathbf{t} = \left(\frac{1}{2}\frac{1}{2}\frac{1}{2}\right)$ . It follows that valence bands at  $\Gamma$  have one more (less)  $e^{-i\pi k/2}$  ( $-e^{-i\pi k/2}$ ) glide eigenvalue than the valence bands at M or R. On the other hand, the band structure along R-X, and along R-Z, where Z is the  $C_3$  partner of X in the  $k_z$  axis, preserves all the compatibility relations; thus Z has the same glide eigenvalues with R and M. Therefore, similar to the case for the  $k_z = 0$  plane, the glide eigenvalues allow a few possible configurations for the ring(s) in the  $k_x - k_y = 0$  plane. For example, there may be a single ring surrounding  $\Gamma$ , or there may be a single ring surrounding M, a single ring surrounding R, and a single ring surrounding Z, and so on. Further band-structure calculation certifies the first case—that is, there is a single ring surrounding  $\Gamma$  in the  $k_x - k_y = 0$  plane. Then, owing to the space-group symmetries, there are in total six nodal rings in the  $k_i \pm k_j = 0$  ( $i \neq j$ ) planes (Extended Data Fig. 1b). Numerical calculations show that the rings in the  $k_i \pm k_j = 0$  ( $i \neq j$ ) planes have a larger radius than the rings in the  $k_i = 0$  planes.

**Topological invariants of  $\text{Zr}(\text{TiH}_2)_2$ .** In order to determine the topological invariants of  $\text{Zr}(\text{TiH}_2)_2$  (space group 227) with the soc setting, we look up its symmetry-indicator set—which is ( $Z_{2w-1}$ ;  $Z_{2w-2}$ ;  $Z_{2w-3}$ ;  $Z_4$ ) = (0002)—in Extended Data

Table 1 and find that there are only two possibilities for the invariants for this symmetry-indicator set. In the first case, the mirror Chern number on the  $\bar{1}\bar{1}0$  plane in the Brillouin zone (the yellow plane in Extended Data Fig. 2a) is 2 (mod 4), whereas in the second case this mirror Chern number is 0 (mod 4). By ab initio calculation, as described in the next paragraph, we find that this mirror Chern number is 0 and thus Zr(TiH<sub>2</sub>)<sub>2</sub> belongs to the second case. In this case, nontrivial TCI invariants include: (i) an hourglass invariant protected by glide symmetry  $\{m_{001}|\frac{1}{4}0\}$ ; (ii) a rotation invariant protected by  $\{2_{\bar{1}\bar{1}0}|000\}$ ; (iii) an inversion invariant; (iv) a screw invariant protected by  $\{4_{001}|\frac{1}{4}\frac{1}{4}\}$ ; and those invariants protected by symmetries equivalent with above symmetries. All of these invariants are  $Z_2$ -type and correspond to either two-dimensional or one-dimensional anomalous surface states.

Here we propose two real space configurations to detect such surface states. In Extended Data Fig. 2c, we show the one-dimensional helical modes protected by screws and/or inversion. The cubic sample is cut out along the (100), (010) and (001) surfaces, all of which are fully gapped. As long as the cube preserves inversion symmetry, there must be an inversion-symmetric one-dimensional helical mode on the boundary, whose shape depends on the experimental situation. However, in presence of the fourfold screw symmetries, which protect nontrivial screw invariants, the shape of helical mode is further constrained. We consider the sample to be large enough such that the fourfold screw symmetry,  $\{4_{001}|\frac{1}{4}\frac{1}{4}\}$ , is preserved on the side surfaces far away from the top and bottom surfaces. Then, as discussed in refs.<sup>9,10</sup>, four one-dimensional helical modes run along the screw axis and transform to each other in turn under the screw operation. Similarly, along any equivalent screw axis there also exist four one-dimensional helical modes. The helical mode shown in Extended Data Fig. 2c is a configuration satisfying all of the above symmetry conditions. In Extended Data Fig. 2d, we show the two-dimensional surface states protected by glide and/or twofold rotation symmetries. The sample is cut out along (110), ( $\bar{1}\bar{1}0$ ) and (001) surfaces, wherein the (001) surface is fully gapped whereas the (110) and ( $\bar{1}\bar{1}0$ ) surfaces are gapless. Owing to the hourglass invariant being protected by  $\{m_{001}|\frac{1}{4}\frac{1}{4}\}$ , the ( $\bar{1}\bar{1}0$ ) surface must have an hourglass mode, and owing to the rotation invariant being protected by  $\{2_{\bar{1}\bar{1}0}|000\}$ , the ( $\bar{1}\bar{1}0$ ) surface must have 2 (mod 4) Dirac nodes. In fact, the two kinds of surface states are consistent with each other: at an even filling number, which is necessary for an insulator in the presence of time-reversal symmetry, the two hourglass crossings protected by glide symmetry also play the role of Dirac nodes for the rotation invariant. Therefore the ( $\bar{1}\bar{1}0$ ) surface has a  $C_2$ -symmetric hourglass mode. The (110) surface has a similar surface state because it is equivalent with the ( $\bar{1}\bar{1}0$ ) surface.

Now let us briefly describe how we calculate the mirror Chern number. First, the parallelogram spanned by  $\mathbf{G}_1$  and  $\mathbf{G}_2$  (Extended Data Fig. 2a) is recognized as the minimal periodic cell in the mirror plane, wherein  $\mathbf{G}_1$  is along the (110) direction and  $\mathbf{G}_2$  is along the (111) direction ( $\mathbf{G}_1$  and  $\mathbf{G}_2$  are reciprocal lattice basis vectors). We therefore calculate the mirror Chern number within this parallelogram. For each point along the  $\Gamma$ - $\mathbf{G}_1$  line,  $k\mathbf{G}_1$ , we define a Wilson-loop matrix as:

$$W_{n,n'}(\mathbf{k}) = \sum_{n_1 n_2 \dots n_{N-1} \in \text{occ}} u_{n, k\mathbf{G}_1} |u_{n_1, k\mathbf{G}_1} + \frac{1}{N} \mathbf{G}_2 u_{n_1, k\mathbf{G}_1} + \frac{1}{N} \mathbf{G}_2 u_{n_2, k\mathbf{G}_1} + \frac{2}{N} \mathbf{G}_2 \dots u_{n_{N-2}, k\mathbf{G}_1} + \frac{N-2}{N} \mathbf{G}_2 |u_{n_{N-1}, k\mathbf{G}_1} + \frac{N-1}{N} \mathbf{G}_2 u_{n_{N-1}, k\mathbf{G}_1} + \frac{N-1}{N} \mathbf{G}_2 | \hat{V}^{\mathbf{G}_2} |u_{n', k\mathbf{G}_1}$$

where  $N$  is a large enough integer to describe the infinite limit;  $|u_{n,k}\rangle$  is the periodic part of the Bloch wavefunction;  $n, n', n_i$  are the valence-band indices; and  $\hat{V}^{\mathbf{G}_2}$  is the embedding operator<sup>61</sup>. For each  $k\mathbf{G}_1$ , we can define the mirror representation matrix as:

$$M_{n,n'}(\mathbf{k}) = u_{n, k\mathbf{G}_1} | \hat{M} | u_{n', k\mathbf{G}_1}$$

where  $\hat{M}$  is the operator of symmetry operation  $\{m_{\bar{1}\bar{1}0}|0\}$ . One can prove that  $M(\mathbf{k})$  always commutes with  $W(\mathbf{k})$ . Therefore, we can project the Wilson-loop matrix into the subspace having mirror eigenvalue  $+i$ ; the mirror Chern number is then given simply by the winding number of the projected Wilson loop. In Extended Data Fig. 2b, we plot the eigenvalues of the projected Wilson-loop matrix as a function of  $\mathbf{k}$ , from which one can find that the winding number is 0.

**Ranking candidate materials.** We rank the candidates in each class of topological materials with each space group by their density of states at the Fermi energy, from low to high, in Supplementary Tables I–V. For materials having zero density of states, we rank them by the size of the energy gap, from large to small. The density of states is obtained from a non-self-consistent calculation by using a  $\Gamma$ -centred Monkhorst–Pack grid with 40  $k$ -points per  $\text{\AA}^{-3}$ , the tetrahedron method for

Brillouin zone integrations, and a number of 5,000 grid points in energy from  $E_f - 4$  eV to  $+4$  eV (where  $E_f$  is the Fermi energy for a material). The gap is extracted from the density-of-states profile, by finding the gap between the tails of the conduction and the valence bands. To be specific, we first find the highest unoccupied energy levels in presence of  $\pm 10^{-3}$  additional electrons per unit cell, and then calculate the gap as the difference of these two levels. The momentum grid that we use for the self-consistent calculation is not large enough to extract an accurate density of states at the Fermi energy, nor is it sufficient to resolve fine features in the density of states as a function of energy. The standard of zero density of states at the Fermi energy applies well to finding good topological insulators and topological crystalline insulators. However, for topological semimetals, this simple standard is not very reliable. Nodal-point semimetals—such as Weyl and Dirac semimetals—should ideally have a Fermi surface that shrinks to discrete points, and the density of states near the Fermi energy should scale as  $-(E-E_f)^2$ . Therefore, it is the functional behaviour, rather than the absolute values, of the density of states that distinguish these semimetal states. Our calculation, as stated above, does not have sufficiently large momentum sampling to reliably extract such functional behaviours. For nodal-line semimetals, the standard is even more irrelevant, as the density of states of ideal nodal-line semimetals should be linearly dependent on the length of the nodal line, which is unknown a priori. We comment that the calculated density of states, and the ranking therein, should only be used as a reference in selecting candidates from the classes of HSPSM, HSLSM and GMSM for further research.

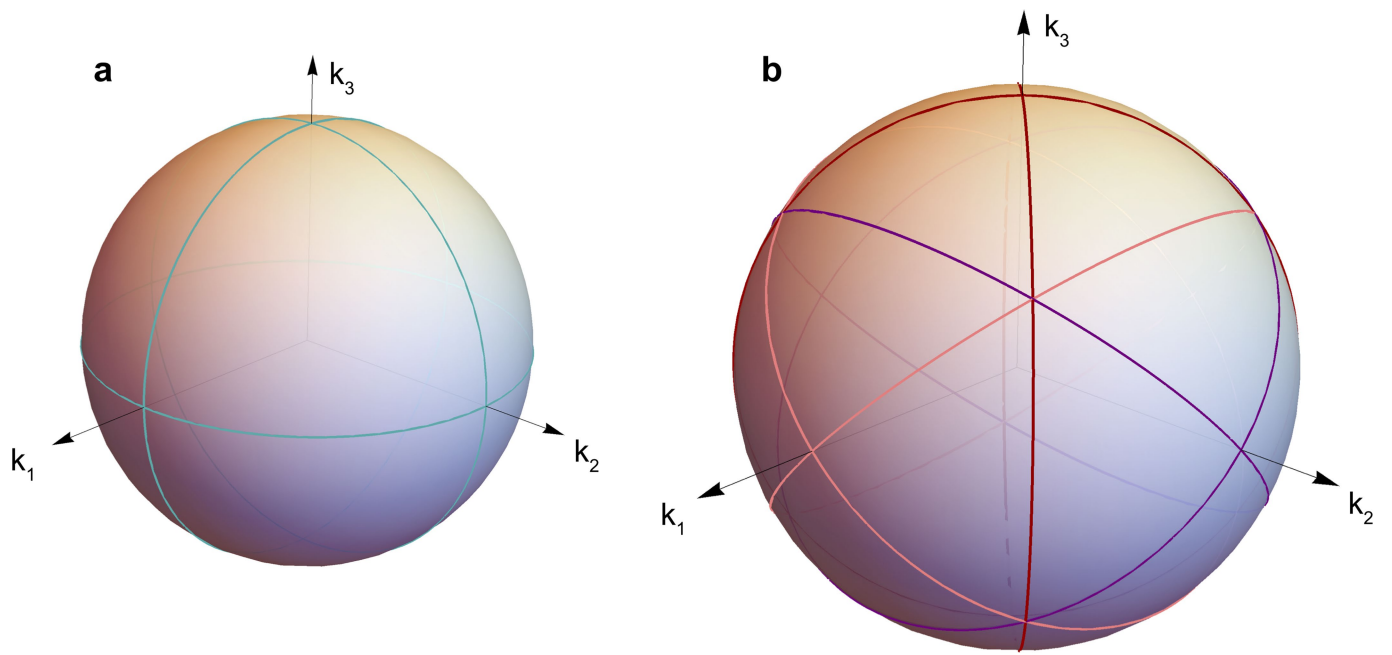
**Topology beyond eigenvalue diagnosis.** Our method, based on the theoretical tools developed in refs.<sup>25–28,30</sup>, is an eigenvalue diagnostic scheme, first introduced in refs.<sup>25,26</sup>. In ref.<sup>26</sup>, it is proved that all of the symmetry eigenvalues at high-symmetry points in a band structure can be mapped to a certain element in a finite group called the symmetry-based indicators. The group structures of indicators are derived in ref.<sup>26</sup>, and their explicit expressions in refs.<sup>27,28,30</sup>. The indicators for each space group, if they exist, are a set of several  $Z_n$  numbers, and they (roughly speaking) quantify how any given symmetry data differ from those of an atomic insulator with the same crystal structure.

The symmetry indicators have the following properties: first, if any indicator is non-zero, the material is not an atomic insulator, that is, it is topologically nontrivial; second, two materials with different indicators are topologically distinct; and third, the topological distinction between two materials that have the same indicators cannot be diagnosed using symmetry data. We note that the third point means that all information on topology that may be extracted from symmetry data has been contained in the values of indicators. One should be aware that the third point implies that there are different topologies that cannot be distinguished using indicators. This is most easily seen in the example of mirror Chern numbers: ref.<sup>28</sup> proves that if two systems have the same indicators, they may differ in the mirror Chern number by  $2n$ , where  $n$  is the order of rotation symmetry in the system. In fact, refs.<sup>27,28</sup> show that mapping from indicators to invariants is one-to-many in general: one given set of indicators maps to several inequivalent sets of topological invariants. Physically, this is because the band inversions can in principle happen away from any high-symmetry point; and given that band inversions may change the topology, there can be two topologically distinct band structures that have identical eigenvalues at all high-symmetry points, rendering powerless any eigenvalue diagnostic scheme. For the same reason, the materials that have zero indicators are not necessarily topologically trivial: we can only say that their topology, if any, is undetectable using our method or any eigenvalue diagnosis.

## Data availability

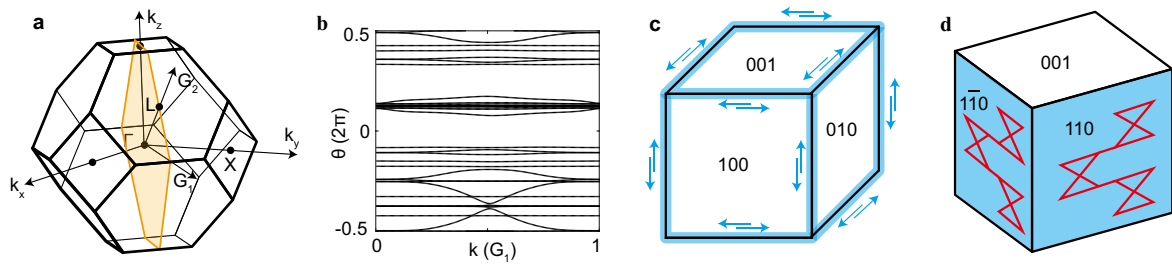
All results are available and searchable with an interactive user interface at <http://materiae.iphyc.ac.cn>. Codes for obtaining the irreducible representations are available from the corresponding author upon reasonable request.

56. Ong, S. P. et al. Python Materials Genomics (pymatgen): a robust, open-source python library for materials analysis. *Comput. Mater. Sci.* **68**, 314–319 (2013).
57. Kresse, G. & Hafner, J. *Ab initio* molecular-dynamics simulation of the liquid-metal–amorphous-semiconductor transition in germanium. *Phys. Rev. B* **49**, 14251 (1994).
58. Kresse, G. & Furthmüller, J. Efficiency of ab-initio total energy calculations for metals and semiconductors using a plane-wave basis set. *Comput. Mater. Sci.* **6**, 15–50 (1996).
59. Kresse, G. & Hafner, J. *Ab initio* molecular dynamics for liquid metals. *Phys. Rev. B* **47**, 558 (1993).
60. Togo, A. & Tanaka, I. First principles phonon calculations in materials science. *Scr. Mater.* **108**, 1 (2015).
61. Alexandradinata, A., Wang, Z. & Bernevig, B. A. Topological Insulators from Group Cohomology. *Phys. Rev. X* **6**, 021008 (2016).



**Extended Data Fig. 1 | Nodal-ring configuration in BaC<sub>20</sub> (nsoc setting).** This material is in space group Pm $\bar{3}$ n. **a**, The three equivalent nodal rings in the  $k_i = 0$  ( $i = x, y, z$ ) planes, protected by the mirror

symmetries on these planes. **b**, The six equivalent nodal rings in the  $k_i \pm k_j = 0$  ( $i, j = x, y, z, i \neq j$ ) planes, protected by the glide symmetries on these planes.



**Extended Data Fig. 2 | Topological invariants and surface states of  $Zr(TiH_2)_2$ .** **a**, Brillouin zone for  $Zr(TiH_2)_2$ , in which the yellow plane is  $m_{1\bar{1}0}$ . **b**, Wilson loop for  $Zr(TiH_2)_2$  in the  $m_{1\bar{1}0}$  plane. **c**, One-dimensional

helical modes in a cubic  $Zr(TiH_2)_2$  sample. **d**, Two-dimensional surface states on each surface of a cubic  $Zr(TiH_2)_2$  sample.

Extended Data Table 1 | Possible invariants for space group 227

$Z_{2,2,2,4}$	weak	$m_{(2)}^{010}$	$g_{\frac{11}{2}0}^{001}$	$g_{\frac{11}{2}0}^{001}$	$g_{\frac{11}{2}4}^{101}$	$2^{001}$	$2^{011}$	$i$	$2_1^{001}$	$2_1^{011}$	$4_1^{001}$	$4_3^{001}$	$\bar{4}^{001}$
0000	000	0	0	0	0	0	0	0	0	0	0	0	0
0000	000	2	0	0	1	0	1	0	0	1	1	1	1
0002	000	0	1	1	0	0	1	1	0	1	1	1	0
0002	000	2	1	1	1	0	0	1	0	0	0	0	1

$Z_{2,2,2,4}$  are the four symmetry-based indicators. The remainder of the labels in the top row refer to topological invariants protected by various lattice symmetries as defined in ref. 27, in which: 'weak' denotes weak topological indices;  $m_{(2)}^{010}$  shows the mirror Chern number which takes a value between  $-1$  and  $+2$ , protected by the (010)-mirror plane;  $G_{abc}^{mnl}$  denotes the  $Z_2$  invariant protected by a glide plane perpendicular to the  $mn$  direction with glide vector  $abc$ ;  $i$  is the  $Z_2$  invariant protected by inversion symmetry about the origin; and  $n_k^{mnl}$  is the  $Z_2$  invariant protected by an  $n$ -fold rotation about the  $mn$  direction followed by a translation along the same direction through the  $k/n$  lattice vector.